A New Concept for High Power RF Coupling between Waveguides and Resonant RF Cavities

Chen Xu[1, *], Ilan Ben-Zvi[1, 2], Haipeng Wang[3], Tianmu Xin[1], and Liling Xiao[4]

Abstract—Microwave engineering of high average-power (hundreds of kilowatts) devices often involves a transition from a waveguide to a device, typically a resonant cavity. This is a basic operation, which finds use in various application areas of significance to science and industry. At relatively low frequencies, L-band and below, it is convenient, sometimes essential, to couple the power between the waveguide and the cavity through a coaxial antenna, forming a power coupler. Power flow to the cavity in the fundamental mode leads to a Fundamental Power Coupler (FPC). High-order mode power generated in the cavity by a particle beam leads to a high-order mode power damper. Coupling a cryogenic device, such as a superconducting cavity to a room temperature power source (or damp) leads to additional constraints and challenges. We propose a new approach to this problem, wherein the coax line element is operated in a TE_{11} mode rather than the conventional TEM mode. We will show that this method leads to a significant increase in the power handling capability of the coupler as well as a few other advantages. We describe the mode converter from the waveguide to the TE_{11} coax line, outline the characteristics and performance limits of the coupler and provide a detailed worked out example in the challenging area of coupling to a superconducting accelerator cavity.

1. INTRODUCTION

Coupling of RF power between waveguides and devices is a fundamental application of microwave engineering. High current particle accelerators are emerging as critical tools for science and applications based on the generation of intense, bright X-rays, powerful neutron sources or high luminosity particle colliders. These machines use superconducting cavities, operating at about 2 to 4 K, at microwave frequencies, to couple the RF power source to the particle beam. To deliver high power RF to the cavity, high average power couplers are needed. A typical coaxial coupler uses a TEM mode to transmit power to a cavity, and both the outer and inner conductors are heated by high RF dynamic loss. Complex cooling systems are used to cool the inner conductor. A careful design is required to minimize both static and dynamic loads of the cryogenic system in which the superconducting cavity resides. Coaxial RF Fundamental Power Couplers (FPC) are often preferable because of their compact size [1]. The compact size allows for the reduction of the static heat load [2, 3]. However, the inner conductor of the coaxial antenna is hard to cool, particularly in a cryogenic environment [4–8]. On the other hand, the outer conductor is easy to cool by employing various thermal anchors. In TEM mode operation, the dynamic RF losses on the inner and outer conductors are inversely proportional to their radii. Increasing the coaxial impedance by reducing the radius of the inner conductor can reduce the total dynamic loss of the TEM coupler system, but exacerbates the cooling of the inner conductor. An additional consideration is the black body radiation from the inner conductor, which loads the cryogenic system, constraining the temperature of the inner conductor.

A typical FPC comprises a waveguide bringing the RF power to close proximity of the cavity, followed by a mode converter to the TEM mode of the coaxial part of the FPC [2]. Coaxial cable can offer a capability for stronger coupling and variable coupling with it compactness. In this paper, we propose a method to reduce the RF dynamic loss and increase the power handling capability of a coaxial coupler as well as its coupling strength to the cavity. The basic idea is to convert the TE_{10} of a rectangular waveguide into a TE_{11} mode of a coaxial transmission line, using a mode converter that will be described in detail. We will show how this approach reduces dramatically the power loss in the center conductor of the coaxial section, thus allowing a higher power handling capability. Another advantage of the TE_{11} coupler is that its mode has an electromagnetic field pattern which couples naturally to the cavity's axial electric field and azimuthal magnetic field or the cavities' higher order modes. Thus, it leads to a lower external Q than a conventional TEM coupler for the same degree of invasiveness. We will show that the TE_{11} coupler has about an order of magnitude stronger coupling to the fundamental mode than the TEM coupler. We also address relevant issues such as the vacuum window, mode polarization anchoring, static and dynamic heat loads, variable coupling, and multipacting.

2. ELECTROMAGNETIC CONSIDERATIONS

The coaxial antenna has several advantages, which explains its popularity. First and foremost, it is compact in size and has a low insertion loss. The RF losses are distributed on both the inner and outer conductor surfaces. The TEM mode field pattern is well known [9]. In this section, we break down the development of the coupler system into several sections: The coaxial section, mode convertor, polarization anchor and final assembly. The electromagnetic simulation is carried out using the ACE 3P simulation package [10]. We provide analytical estimates as well as numerical simulations for a specific design.

2.1. The TEM Transmission Line

The electromagnetic fields of TEM mode have an azimuthal symmetry; thus, the magnetic field H is uniform on either conductor surface, and the azimuthal H field is inversely proportional to the distance from the axis of symmetry. Therefore, the losses on the inner and outer conductors are inversely proportional to the radii of the conductors. With a coaxial line with inner conductor and outer conductor radii a and b, we can get characteristic impedance Z, the attenuation coefficient α, and peak electric field E_{peak} of this structure in Eq. (1).

$$
\begin{aligned}
Z &= \frac{1}{2\pi}\sqrt{\frac{\mu}{\varepsilon}}\ln\frac{b}{a} \approx 60\,\Omega\ln\frac{b}{a} \\
\alpha &= \frac{R_s}{2\eta}\frac{a^{-1}+b^{-1}}{\ln\frac{b}{a}} \\
E_{peak} &= \sqrt{\frac{\eta P_{in}}{\pi a^2 \ln\frac{b}{a}}}
\end{aligned}
\tag{1}
$$

where R_s is the surface resistivity on the conductors, $\eta = (\mu/\varepsilon)^{1/2} \sim 377\,\Omega$, and a, b are the inner and outer conductor radii.

These expressions can be used to evaluate the total power loss along the coax line. Using the state of art 1.3 GHz outer conductor radius 46 mm as a constant [7, 8], the attenuation rates are 27.2 dB/m and 25.6 dB/m for impedances of 75 Ω and 30 Ω, respectively. The peak E fields are 3.38×10^5 V/m and 2.67×10^5 V/m, respectively, for a forward RF power of 200 kW.

2.2. The TE_{11} Transmission Line

The power limit imposed by the TEM mode of the coaxial transmission line can be overcome. The RF power delivery of the TEM mode is limited by the cooling capacity of the inner conductor. Currently, the limit on the CW RF power is 115 KW at 1.3 GHz [8]. Instead of the TEM mode, we propose to use
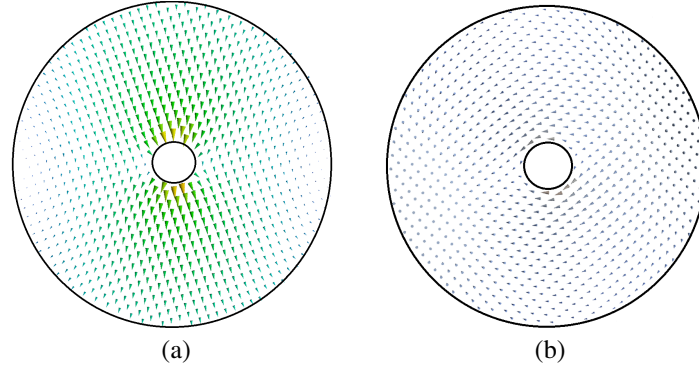
Figure 1. (a) Electric and (b) magnetic field vectors and respectively) of the TE_{11} mode in a coaxial transmission line. The black curves represent the metal (perfect electric conductor) boundary conditions.

a higher order mode in the coaxial cable to deliver the RF power. In particular, we choose the TE_{11} coaxial mode. The electric and magnetic fields of TE_{11} mode electromagnetic field configurations are illustrated in Fig. 1.

The TE_{11} coaxial mode cutoff frequency is determined by inner and outer conductor radii, (a and b, respectively) and is given by the condition $k > k_c$, where $k = 2\pi/\lambda$ and $k_c \approx 2/(a + b)$ are the propagation constants in free space and in the coaxial transmission line, respectively. Therefore, we obtain $a + b > \lambda/\pi$. Substituting this k_c into the expressions for the magnetic field on both surfaces, we get expressions for the attenuation rate, impedance and peak E field of TE_{11} coaxial mode shown in Eq. (2) [See Appendix A for a detailed derivation]:

$$Z = \frac{E_\rho}{H_\phi} = \frac{\omega\mu}{\beta} = \frac{\eta k}{\beta}$$

$$\alpha = \frac{R_s \left\{ a \left[k_c^4 + \frac{\beta^2}{a^2} \right] (J_1(k_c a) + \gamma Y_1(k_c a))^2 + b \left[k_c^4 + \frac{\beta^2}{b^2} \right] (J_1(k_c b) + \gamma Y_1(k_c b))^2 \right\}}{\eta k \beta \left\{ [J_1(k_c b) + \gamma Y_1(k_c b)]^2 [(k_c b)^2 - 1] - [J_1(k_c a) + \gamma Y_1(k_c a)]^2 [(k_c a)^2 - 1] \right\}} \quad (2)$$

$$E_{peak} = \frac{2[J_1(k_c a) + \gamma Y_1(k_c a)]}{\left\{ [J_1(k_c b) + \gamma Y_1(k_c b)]^2 [(k_c b)^2 - 1] - [J_1(k_c a) + \gamma Y_1(k_c a)]^2 [(k_c a)^2 - 1] \right\}^{\frac{1}{2}}} \sqrt{\frac{\eta k P_{in}}{a^2 \beta}}$$

where γ, as shown in Appendix A, is a function of the two radii, and β is the propagation constant in the coaxial transmission line.

One interesting feature of the TE_{11} mode is that the power dissipation on the inner conductor can be much smaller than that on the outer conductor. This feature allows us to significantly increase the power limit of the coaxial transmission line. Varying the radii a and b will change the propagation constant and the guided wavelength of the TE_{11} mode in the coaxial cable. Consequently, the dissipated power on both inner and outer conductor, the peak electric field also changes. The derivation provided in Appendix shows that choosing a smaller a/b ratio could reduce the RF loss on the inner conductor, the total attenuation rate and the peak surface electric field. The peak electric field at 1.3 GHz is an order of magnitude lower than the Kilpatrick breakdown field [11]. We find that a smaller a/b ratio is preferred to minimize the inner conductor loss, increase the impedance and reduce the total loss with affordable peak electric field increase. However, a larger b will be needed to propagate TE_{11} mode in a coaxial cable when inner conductor is smaller. In some cases, if the cryogenic system has capability and coupler dimension is limited, one can increase the a/b ratio and compromise some cryogenic loss for the coupler dimension. On the other hand, if the coupler dimension has little limitation, such as in our case, we can minimize the a/b ratio to minimize the inner conductor loss. We will describe this design in the next section.

3. HIGH POWER TE$_{11}$ COUPLER DESIGN

3.1. Choice of Parameters for the TE$_{11}$ Transmission Line

The optimal choice for the radii a and b is best shown using an example. We elect to use a coaxial fundamental power coupler at a frequency of 1.3 GHz, for which there are a few designs for high power coupler to superconducting RF cavities. Firstly, to ensure propagation, we must observe the condition $a/b > \lambda/\pi b - 1$. Next, we have freedom to pick up the inner conductor radius. Here we choose to keep the inner conductor radius as 15 mm, which is similar to existing couplers. The minimal outer conductor radius is 60 mm to ensure propagation of the 1.3 GHz RF wave. At this set of radii, the transmission line propagation constant β is real but small, which suggests that the guided wavelength is long. When we further increase the outer conductor radius, β increases, and the dynamic loss on both inner and outer surface changes. Thus, we choose the outer conductor radius as 70 mm, change the inner conductor radius and find the dynamic loss on both inner and outer conductors. Since there is some freedom in the choice of the conductor radii, it is best to illustrate the functional dependence of the power deposition on the inner and outer conductors as we vary the radii, which we do in Fig. 2. Staying with the numerical choice, Fig. 3 is evaluated at 1.3 GHz, and we pick the conductivity to be that of room temperature Cu. We simulate pure transmitted RF power with no reflection.
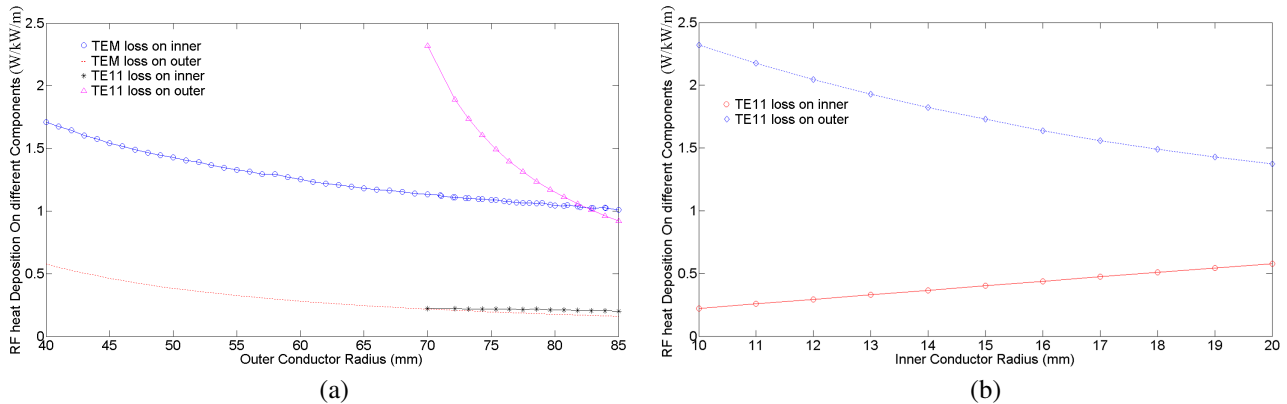

Figure 2. Power loss fraction of coaxial transmission lines in TEM and TE$_{11}$ modes. The unit is W/kW/m (the power loss in watts for a unit length coaxial transmission line given the RF power flow of 1 kW.) (a) The power loss fraction as a function of the radius of the outer conductor for a fixed inner conductor radius of 15 mm. The red dot line represents the outer conductor of a TEM mode; the pink triangles represent the outer conductor of the TE$_{11}$ mode; the blue circles represent the inner conductor of the TEM mode; and the black stars represent the inner conductor of the TE$_{11}$ mode. (b) The power loss fraction on the inner (red circles) and outer conductor (blue square) of the TE$_{11}$ mode as function of the inner conductor radius for a fixed outer conductor radius of 70 mm.

Figure 2(a) shows that the dynamic loss on the inner conductor in the TE$_{11}$ mode (black stars) is significantly lower than the inner conductor loss in the TEM mode (blue circle), while the outer conductor loss is comparable. This figure also suggests that a large outer conductor is preferable ($b \geq 70$ mm), but for practical reasons we would like to keep this radius smaller than the large edge of a standard rectangular WR650 waveguide whose dimension is 6.5 Inches [165.1 mm] $\times 3.25$ Inches [82.55 mm]. Fig. 2(b) suggests that a smaller inner conductor will reduce the inner conductor loss and increase outer conductor loss; however, at this point we prefer to stay with the 15 mm chosen above. Thus, in this example, we will use the inner and outer conductor radii as 15 mm and 70 mm, respectively. Thus, the cutoff frequency of this design is 1.12 GHz.

At this point it is worth observing another interesting feature of the TE$_{11}$ mode transmission line, which is the possibility of using an elliptical cross section. An elliptical cross section lowers the cutoff frequency of the desired polarization and allows reducing the coaxial coupler dimensions. Another advantage of this shape is that we can intentionally cut off the other TE$_{11}$ polarization to maintain mode

purity. However, the mode convertor design described below must guarantee that only one polarization will be excited. By doing that, we can propagate the 1.3 GHz RF wave, fix the polarization orientation and further reduce the size of the coupler based on this transmission line. To align the ellipse coaxial cable with standard rectangle waveguide, the ellipse ratio is 0.5 above which the inner conductor loss rate reaches a plateau. The elliptical coaxial line design is not a necessity for this specific application, but one can also use the circular coaxial cable without any mode purity compromise.

At 1.3 GHz, we observe a significant reduction of the power deposition on the inner conductor of the TE_{11} coupler compared with the conventional TEM coupler, while all other parameters such as the total attenuation and peak surface electric field remain practically unchanged. We summarize the comparison between different coaxial modes in Table 1.

Table 1. The electromagnetic parameters.

Specifications	TEM (30 Ω)	TEM (75 Ω)	TE_{11} (Circular)	TE_{11} (Elliptical)
a (mm)	28	13	15	15
b (mm)	46	46	70	70
Loss on the inner Conductor (W/kW/m)	1.74	1.52	0.40	0.77
Total Attenuation (dB/m)	25.6	27.2	26.3	25.2
E_{peak} at 200 kW (V/m)	2.67×10^5	3.38×10^5	3.96×10^5	5.1×10^5

Comparison of the electromagnetic parameters for a few examples of coaxial transmission lines. The advantage of the TE_{11} mode is a significant reduction of the power loss on the inner conductor.

3.2. The Mode Convertor

The power delivery from the RF source is usually done with a standard rectangular waveguide. The RF power is delivered in the TE_{10} mode, which is the fundamental mode of a rectangular waveguide. It is convenient to transfer the RF power from TE_{10} rectangular mode to the TE_{11} mode coaxial antenna, given that both are dipole modes. We designed a compact mode converter to achieve this transformation. The converter is a two-port, three-mode system as illustrated in Fig. 3.
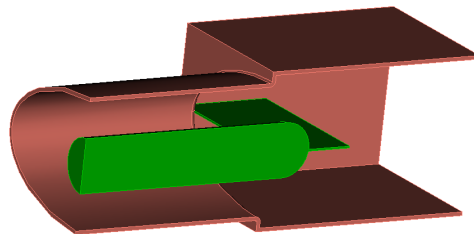

Figure 3. Cross-section view of the rectangular to coaxial mode convertor. The electric field in TE_{11} is in the vertical direction.

The regular waveguide, which is standard WR650 waveguide, supports TE_{10} mode, while the coaxial port supports two modes: TEM and TE_{11}. We want to convert the TE_{10} mode power to the TE_{11} mode with a negligible leakage to the TEM mode of the coaxial port. We use a perturbation method to design the convertor. On the right-hand side, in the rectangular waveguide, we insert a thin plate in the horizontal center, and it will not disturb the TE_{10} mode in the rectangular waveguide. On

the left-hand side, that of the circular or elliptical coaxial transmission line, we have the inner conductor. In the transition area, we use a smooth second order parabola convex function to connect the thin plate to the inner conductor terminus. The return loss is minimized through numerical optimization of the length of the transition. We plot the S parameters of this convertor in Fig. 4. We label the scattering parameters $S(M1, N1 : M2, N2)$ where M represents the port number, and N represents the mode number on that port. Port 1 is on the rectangular waveguide in Fig. 3, and Port 2 is in the coaxial section. We number the modes as follows: Mode 1 in the rectangular waveguide is the TE_{10}, while modes 1, 2 and 3 in the circular waveguide are the TEM mode, the vertical and the horizontal polarizations of the TE_{11} mode, respectively. We choose the insertion distance as 10 mm for the lowest return loss yet low TEM mode content in the elliptical coaxial cable. The leakage to the TEM mode is negligible at less than -35 dB (red), and reflection is also less than -25 dB (black).

From Fig. 4, we choose the minimal return loss and give the scattering matrix of this convertor in Table 2. In this table, the cell at the *2, 1 column and 1, 1* row is -38.9 dB indicating the absence of the TEM mode in the transmitted signal. The *2, 3 to 1, 1* cell value of -89.6 dB indicates the purity of the polarization.

Table 2. Scattering parameters.

Port, Mode:	1, 1	2, 1	2, 2	2, 3
1, 1	-25.5	-38.9	-0.0129	-89.6
2, 1	-38.9	-0.00116	-38.6	-72.3
2, 2	0.0129	-38.6	-25.5	-89.4
2, 3	-89.6	-72.4	-89.4	-61.6

The mode convertor scattering parameters, the Port and Mode labels are defined in the text. The frequency is 1.3 GHz. The units are in dB.

Also, we scan the scattering parameter and investigate the convertor's bandwidth. The results are shown in Fig. 5. Below the cutoff frequency, no propagation of TE_{11} mode is observed.
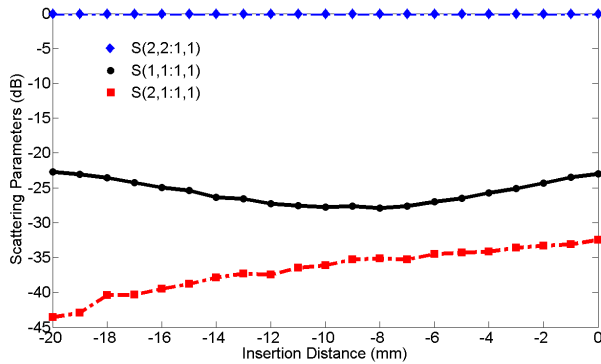

Figure 4. Scattering parameters are plotted as a function of the length of the plate in the mode converter. $S(1, 1 : 1, 1)$ is drawn in black circles; $S(2, 1 : 1, 1)$ is red squares; $S(2, 2 : 1, 1)$ is blue diamonds.
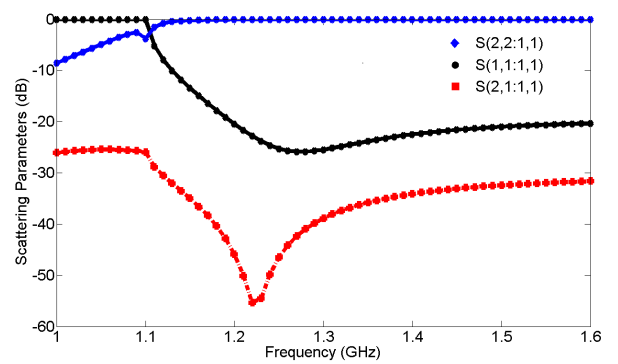
Figure 5. Frequency spectrum of the scattering parameter and phase difference of the convertor. The S parameters are plotted in colors. $S(1, 1 : 1, 1)$ is black; $S(2, 1 : 1, 1)$ is red; $S(2, 2 : 1, 1)$ is blue.

3.3. Full Assembly and Coupling to the Cavity Resonator

The coaxial coupler with TEM mode utilizes the standard door-knob convertor, while the coaxial coupler with TE_{11} mode utilizes the mode converter described above. To accommodate the conventional orientation of the waveguide, we add an optional a standard E-bend rectangular waveguide element.
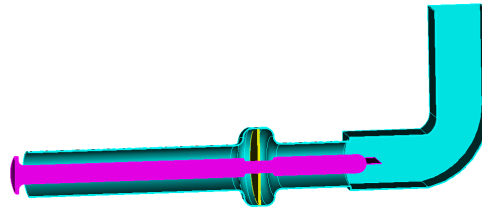
Figure 6. Cross-section of the final Assembly of the TE_{11} elliptical coaxial coupler.

Table 3. Scattering parameters.

Port, Mode:	1 : 1	2 : 1	2 : 2	2 : 3
1 : 1	−24.9	−38.3	−0.0244	−62.0
2 : 1	−38.3	−0.0134	−38.3	−86.7
2 : 2	−0.0244	−38.3	−24.9	−62.3
2 : 3	−62.0	−86.7	−62.3	−57.2

The mode convertor scattering parameters. the Port and Mode labels are defined in the text. The frequency is 1.3 GHz. The units are in dB.

We also add a smooth transition to match the RF power without multipacting, and this type of window is used by the IPO and ESS projects' high power couplers [12, 13]. The full assembly is demonstrated in Fig. 6. The scattering matrix is given in Table 3.

4. THERMAL DESIGN

4.1. Contemporary TEM Coupler

A contemporary conventional TEM coupler was designed to accommodate power on the order of 115 kW at 1.3 GHz CW RF power [8]. Usually, the peak electric field is not the limiting factor for the high power operation, but the thermal concerns limit the maximum power capability. An active cooling system (usually water) must be applied to the inner conductor. These anchors' locations are optimized for the TEM coupler, and they might not be optimal for the TE_{11} coupler. The schematic thermal anchor locations are illustrated in Fig. 7. The thermal anchors flanges are connected to the different temperatures: 2 K, 5 K, and 70 K. The coaxial sections between the window and waveguide sections are all thermally anchored to a chilled water pipe at 300 K. The waveguide is also thermally anchored to the chilled water pipe. The coupler outer conductor is made from Cu plated stainless steel. The stainless-steel thickness is 2 mm. Both couplers require 10 μm thick copper plating on the outer conductor to reduce the RF dynamic and static loss. The inner conductors are made from oxygen-free copper.
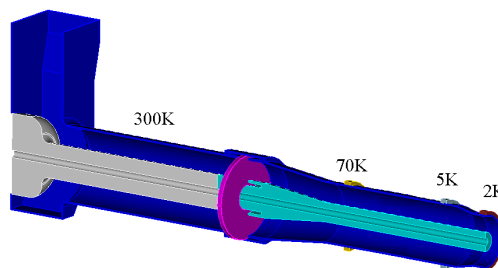

Figure 7. Cross-section view of TEM Couplers and the schematic scheme of the thermal anchors locations.

The water supply radius is 5 mm, with water flow of 0.25 gallon/min, and the convection coefficient is $300 \, \text{W/m}^2/\text{K}$. The recent simulation suggests that this coupler can successfully transmit 115 kW power, but the inner conductor surface temperature exceeds 100C° when $\sim 230 \, \text{kW}$ power is transmitted.

4.2. TE$_{11}$ Coupler Thermal Anchors

Given that the TE$_{11}$ coaxial coupler has a lower dynamic loss in the inner conductor, we use this feature to eliminate the water-cooling. In the next sections, we will study the static and dynamic losses in a traveling wave mode operation [8]. As before, we use the example of a 1.3 GHz coupler to a superconducting cavity. To conduct a fair comparison, the two couplers have the same length, and the thermal anchor locations on both couplers are at the same locations in Fig. 8. No active water cooling is installed inside the inner conductor of TE$_{11}$ coupler, while a recirculating water cooling system is installed in the TEM coupler. We can further reduce the couplers dynamic loss by introducing a thermal anchor to the inner conductor. From Fig. 1, we see that one feature of the TE$_{11}$ coaxial mode is that the horizontal plane has a perfect electric boundary condition. Therefore, we can insert a metal plate without compromising the RF performance, but this plate can be used to anchor the temperature of the inner conductor to the outer conductor by thermal conduction. Thus, the temperature of inner conductor will be reduced to a lower temperature and further reduce the dynamic loss. However, this flat plate will slightly increase the dynamic loss. Such a feature is not available on TEM couplers, i.e., inserting a flat plate will destroy the TEM field pattern. We illustrate the design in Fig. 8 where the inner conductor is connected to 80 K thermal anchor outside.
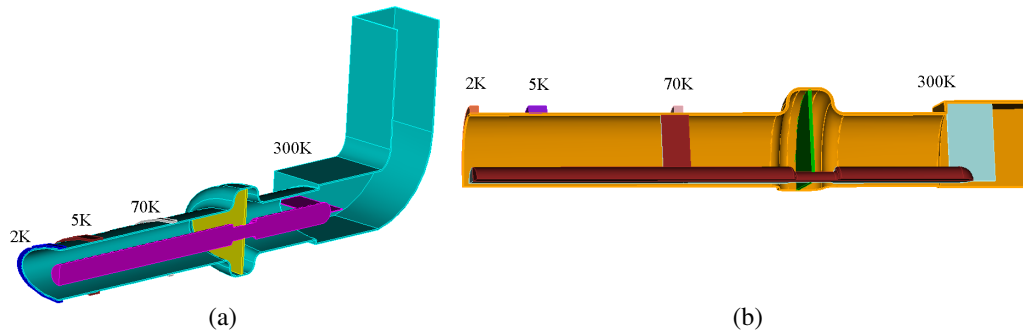

Figure 8. (a) Cross-section viewof TE$_{11}$ Couplers and the schematic scheme of the thermal anchors locations. (b) A cross-section view of the inner conductor thermal anchors is added on the TE$_{11}$ couplers.

In the following, we will investigate the temperature profile when the coupler transfers 200 kW RF power without reflection in the TEM and TE$_{11}$ configurations shown in Fig. 7 and Fig. 8, respectively. The multi-physics simulations are conducted by the ACE3P software [10]. The following simulations include the temperature dependence of the RF surface resistance.

4.3. Static Loss

We investigate the static thermal heat load (RF power off) to different thermal anchors. For the TEM coupler (Fig. 7), the water-cooling ambient temperature is 290 K. The TE$_{11}$ coupler (Fig. 8) does not require water-cooling for the center conductor. For the TEM coupler, the outer conductor and upper part of the inner conductor are copper plated, and the bottom part is pure copper, while for TE$_{11}$ coupler, the center conductor is made of OFHC copper. The temperature profiles of both cases are illustrated in Fig. 9.

From the ACE3P simulation, we obtain the temperature distribution and heat flow to the various anchor points for both cases. We compare the results in Table 4. The static loss figures for the TE$_{11}$ coupler are comparable to the conventional TEM couplers, but the TE$_{11}$ coupler system does not employ water cooling.
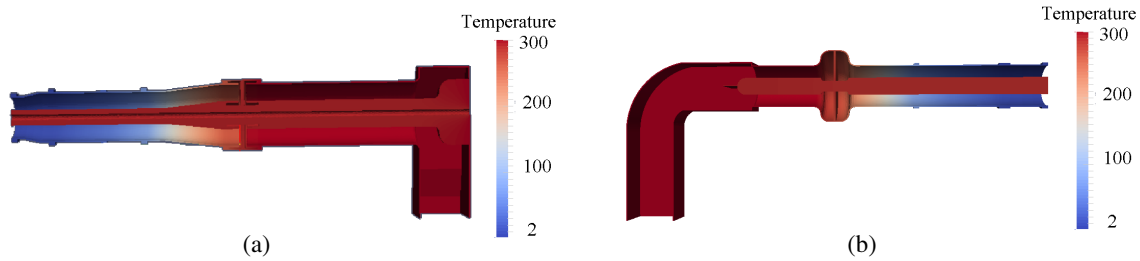
Figure 9. RF power off temperature profiles of the (a) TEM and the (b) TE_{11} coaxial couplers. The thermal anchors are placed at the same location on the couplers' outer conductors as shown in Figs. 7 and 8.

Table 4. Statics loss.

Static Loss (W) on the anchors	TEM	TE_{11}
2 K	0.264	0.167
5 K	1.841	2.572
70 K	8.434	16.626
300 K	−35.909	−17.996
Water Cooling	25.370	N/A

The comparison of the statics loss to the different thermal archers.

The most critical comparison is the heat flow to the 2 K and 5 K anchors. The results are comparable and that suggests that this coupler design has a satisfactory 2 K heat load.

4.4. Dynamic Loss

Here we investigate the temperature profile when the coupler transfers 200 Kw RF power with no reflection. This means that the RF power is transferred to the beam with a critical coupling. For both cases, the warm alumina windows have a relative emissivity ~ 9, and its loss tangent is 10^{-5}, while the copper film electric residual resistivity ratio (RRR) is taken as 5. As shown in Fig. 10, the temperature profiles of both couplers are provided when both couplers deliver 200 kW in a travelling wave mode.

With improved cooling of the outer conductor, the TE_{11} mode will exhibit reduced dynamic loss because of the thermal feedback on the surface resistance. The door-knob convertor of the TEM coupler is expected to have larger dynamic loss than the TE_{11} converter, because of its larger size. Therefore, the total dynamic loss for the TE_{11} coupler is smaller than the TEM coupler. Fig. 10 shows that the
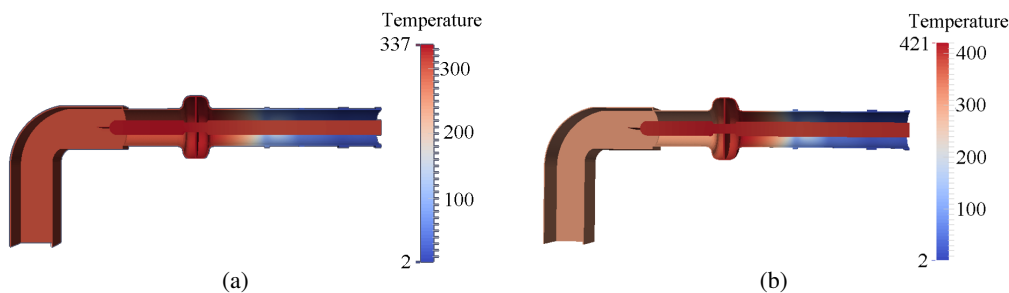

Figure 10. Temperature profiles of the TE_{11} coupler, at transmitted power levels of (a) 115 kW and (b) 200 kW (with no reflection).

maximum temperatures are $337\,\mathrm{K}$ and $421\,\mathrm{K}$ for TE_{11} couplers at $115\,\mathrm{kW}$ and $200\,\mathrm{kW}$, and these are acceptable in terms of thermal radiation [15]. We also estimate the black body radiation in this TE_{11} coupler. The emitted power from a heat body to the cold environment is given as: $Q = \varepsilon \sigma A (T^4 - T_0^4)$ where ε is the emissivity (1×10^{-2}), σ the Stefan-Boltzmann constant $(5.670367 \times 10^{-8}\,\mathrm{Wm^2K^4})$, A the surface area $(0.025\,\mathrm{m^2})$, and T and T_0 are the tip and environment temperatures. In our case, the upper limit of the emitted power is $0.425\,\mathrm{W}$ when the coupler tip temperature is $350\,\mathrm{K}$. Based on the tip, temperatures are $337\,\mathrm{k}$ and $421\,\mathrm{K}$ when it transmits $115\,\mathrm{kW}$ and $200\,\mathrm{kW}$ RF power, and we obtain the maximum emitted power $0.366\,\mathrm{W}$ and $0.445\,\mathrm{W}$, respectively.

The total dynamic loss in Table 5 considers the temperature dependencies of the electric and thermal resistivity. The dynamic loss values are $235\,\mathrm{W}$ and $405\,\mathrm{W}$ for $115\,\mathrm{kW}$ and $200\,\mathrm{kW}$ transmitted RF power, respectively, in the TE_{11} coupler. It is illustrated that the TE_{11} coupler has a lower dynamic loss than the conventional TEM couplers in Table 5. The total dynamic loss is reduced to 40% of dynamic loss of TEM coupler. The $2\,\mathrm{K}$ and $5\,\mathrm{K}$ losses are comparable. Those thermal anchors heat fluxes are slightly increased from the TEM coupler, because the dynamic loss, which is locally generated on the outer conductor, is directly damped to the thermal anchors. The flux distribution is dependent on the anchors location optimizations. We can further optimize the cooling scheme for this TE_{11} coupler to reduce the $2\,\mathrm{K}$ and $5\,\mathrm{K}$ heat flux.

Table 5. Dynamic loss.

Dynamic Loss on the anchors (W)	TEM (115 kW)	TEM (200 kW)	TE$_{11}$ (115 kW)	TE$_{11}$ (200 kW)
2 K	0.656	0.871	0.772	1.024
5 K	3.025	3.943	5.877	8.338
80 K	15.994	22.376	111.932	166.615
300 K	165.685	314.692	116.484	228.806
Water Cooling	293.496	488.436	N/A	N/A
Total Loss	478.856	830.317	235.064	404.783

This table shows the budget of the total thermal flux to each anchor. The total power flow into the system comprise of dynamic loss and static loss. The TE$_{11}$ coupler has 50% of the total dynamic loss power than the conventional TEM coaxial coupler.

5. PRACTICAL CONSIDERATIONS

5.1. Coupling to a Cavity

When the beam loading is high, the external Q of couplers must be small to match the loaded Q of the cavity. At the power levels of hundreds of kW, the external Q is around $10^4 \sim 10^5$. Moreover, the couplers should have limited beam kick by reducing the coupler insertion length. To achieve that, we use the tip shape design, which was first introduced by Cornell University [16]. The coupling of TE_{11} mode is significantly stronger than TEM mode for the same degree of tip penetration. This is an important advantage. Taking a single cell $1.3\,\mathrm{GHz}$ cavity as an example, we design this cavity for eRHIC project in BNL [17]. The cavity has a long taper on each side of the cavity to minimize the beam loss factor. However, the long taper makes it difficult to achieve the necessary strong coupling. We installed two couplers on this cavity at the same location of TEM couplers to compare their coupling strength, and the schematic is shown in Fig. 11.

The external Q as a function of insertion length for both couplers is simulated and plotted in Fig. 12. Compared with TEM couplers, the TE_{11} coaxial coupler requires smaller insert length. Note that to achieve an external Q of 2e5, the insertion length of the TEM coupler will be larger than that of the TE_{11} coupler by $\sim 25\,\mathrm{mm}$. This is another advantage of this design.
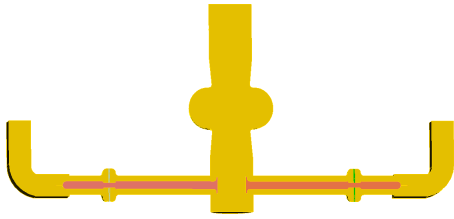
Figure 11. Cross-sectional view of two coaxial couplers installed on a single cell cavity. To compared with conventional TEM couplers, TE_{11} elliptical coaxial coupler are installed to the same location for a fair comparison.
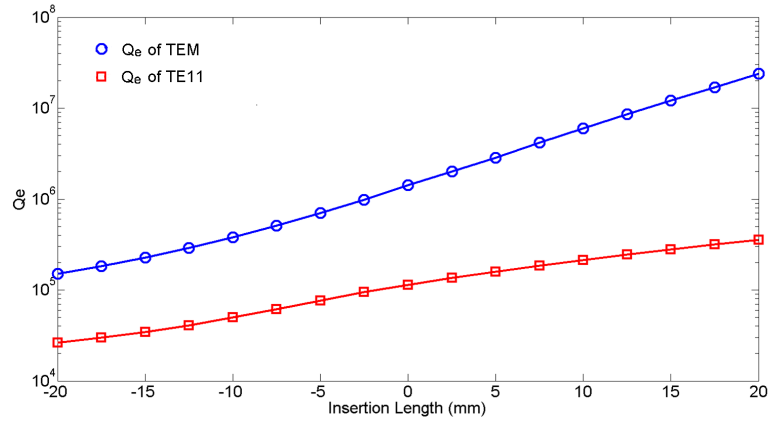
Figure 12. External Q changes with the FPC insertion length. The red squares and blue circles are Q_e for the TE_{11} and the TEM couplers, respectively.

5.2. Multipacting Simulation

Track3p code simulates the possibility of multipacting [10]. We use the secondary yield curve of an oxygen-free copper and sapphire windows to conduct this simulation at different forward RF power levels. This simulation is performed to predict the power levels at which multipacting might occur and to identify the locations. Fig. 13 shows that particle count number (representing the strength of the multipacting) increases at various forward RF power levels. The multipacting simulation is done when the forward RF power ranges from 10 kW to 200 kW in 10 kW steps. We found no significant multipacting barriers, partially because the TE_{11} design avoids the choke design where multipacting usually happens [18].
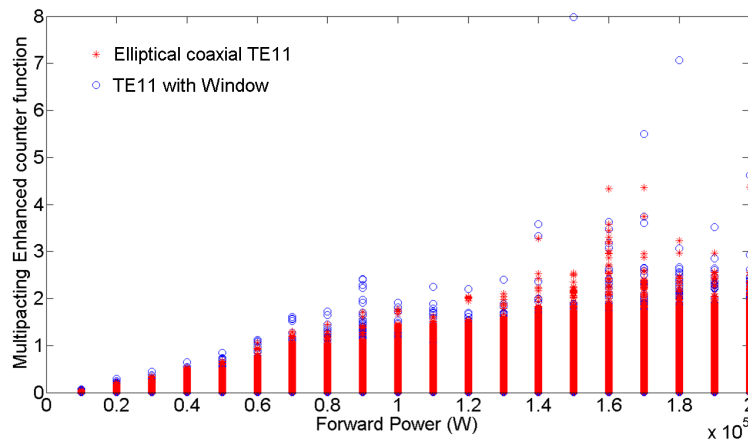

Figure 13. Electron counter number at steady state as a function of the forward RF power level. No significant multipacting barriers are found for this TE_{11} coupler design. The red stars and blue circle are the multipacting enhancement factor for elliptical coaxial section and window sections respectively.

6. CONCLUSION

In this report, we propose a new type of TE_{11} couplers for high power SRF linac. This new coupler uses coaxial TE_{11} mode to transmit RF power, and it can deliver higher forward RF power without complex water-cooling system. The TE_{11} coupler is compact at high frequencies, above approximately $1\,\mathrm{GHz}$, but at lower frequencies its dimensions grow due to the cutoff frequency of this mode. This coupler has $> 40\%$ of the total RF loss of a conventional TEM coupler at the same forward RF power. Its static loss is comparable to a conventional TEM coupler. This coupler can handle higher RF power than the example given if active cooling of the inner conductor is added. In addition, the TE_{11} coupler has about an order of magnitude stronger coupling to a cavity than a similarly placed TEM coupler.

APPENDIX A. STUDY OF THE TE_{11} COAXIAL MODE

The general form of a Transverse Electric (TE_{nm}) electromagnetic field of angular frequency ω in a coaxial transmission line is shown in Eq. (A1):

$$
\begin{aligned}
H_z(\rho,\phi,z) &= e^{-i\beta z}(A\sin n\phi + B\cos n\phi) \times (CJ_n(k_c\rho) + DY_n(k_c\rho)) \\
E_z(\rho,\phi,z) &= 0 \\
E_\phi(\rho,\phi,z) &= \frac{i\omega\mu}{k_c}e^{-i\beta z}(A\sin n\phi + B\cos n\phi) \times (CJ'_n(k_c\rho) + DY'_n(k_c\rho)) \\
E_\rho(\rho,\phi,z) &= \frac{i\omega\mu n}{k_c^2\rho}e^{-i\beta z}(A\cos n\phi + B\sin n\phi) \times (CJ_n(k_c\rho) + DY_n(k_c\rho)) \\
H_\rho(\rho,\phi,z) &= \frac{i\beta}{k_c}e^{-i\beta z}(A\sin n\phi + B\cos n\phi) \times (CJ'_n(k_c\rho) + DY'_n(k_c\rho)) \\
H_\phi(\rho,\phi,z) &= \frac{i\beta n}{k_c^2\rho}e^{-i\beta z}(A\cos n\phi + B\sin n\phi) \times (CJ_n(k_c\rho) + DY_n(k_c\rho))
\end{aligned}
\tag{A1}
$$

Where Z, ϕ and ρ represent the cylindrical coordinates, and A, B, C and D are constants to be determined by the boundary conditions and amplitude of the field. J_n, Y_n are the n'th order Bessel functions of the first and second kind, and (') represents the derivative with respect to the argument. β and k_c are the guided wave number and the cutoff wave number.

The impedance of the TE modes is given in Eq. (A2):

$$
Z = \frac{E_\rho}{H_\phi} = \frac{\omega\mu}{\beta} = \frac{\eta k}{\beta}
\tag{A2}
$$

Here $\eta = 377\,\Omega$ and $\omega\mu = \eta k$. When we consider just one polarization, we can set $B = 0$. In the following, we will drop the z dependency and choose the $n = 1$ mode. Thus the TE_{11} field in the coaxial transmission line is given in Eq. (A3):

$$
\begin{aligned}
H_z(\rho,\phi) &= A\sin\phi \times (CJ_1(k_c\rho) + DY_1(k_c\rho)) \\
E_z(\rho,\phi) &= 0 \\
E_\rho(\rho,\phi) &= \frac{i\omega\mu}{k_c^2\rho}A\cos\phi \times (CJ_1(k_c\rho) + DY_1(k_c\rho)) \\
E_\phi(\rho,\phi) &= \frac{i\omega\mu}{k_c}A\sin\phi \times (CJ'_1(k_c\rho) + DY'_1(k_c\rho)) \\
H_\rho(\rho,\phi) &= \frac{i\beta}{k_c}A\sin\phi \times (CJ'_1(k_c\rho) + DY'_1(k_c\rho)) \\
H_\phi(\rho,\phi) &= \frac{i\beta}{k_c^2\rho}A\cos\phi \times (CJ_1(k_c\rho) + DY_1(k_c\rho))
\end{aligned}
\tag{A3}
$$

Now we apply the boundary conditions of a perfect conductor at the surfaces bounded by a and b, and the inner and outer conductor's radii in Eq. (A4).

$$
E_\phi(a,\phi) = E_\phi(b,\phi) = 0
\tag{A4}
$$

Thus we obtain the linear equations in Eq. (A5):

$$CJ'_1(k_c a) + DY'_1(k_c a) = 0$$
$$CJ'_1(k_c b) + DY'_1(k_c b) = 0 \tag{A5}$$

These equations have non-zero solutions for C and D only when the determinant equals zero in Eq. (A6).

$$\det \begin{bmatrix} J'_1(k_c a) & Y'_1(k_c a) \\ J'_1(k_c b) & Y'_1(k_c b) \end{bmatrix} = 0 \tag{A6}$$

By solving this equation, we can obtain k_c numerically for a given set of a and b. A empirical solution is shown in Eq. (A7).

$$k_c \approx \frac{2}{a+b}$$
$$\gamma = -\frac{J'_1(k_c a)}{Y'_1(k_c a)} = -\frac{J'_1(k_c b)}{Y'_1(k_c b)} \tag{A7}$$

Now, we can discuss the major specifications of the TE_{11} mode and compare them with TEM mode. The most important three parameters are:

1. RF loss on the inner and outer conductors.
2. Total attenuation rate.
3. The peak surface electric field.

APPENDIX B. RF LOSS ON THE INNER AND OUTER CONDUCTORS

The ratio of the azimuthal and longitudinal components of the vector H field are given in Eq. (B1).

$$\overrightarrow{H_{total}} = \overrightarrow{H}_z + \overrightarrow{H}_\phi$$
$$\left| \frac{H_\phi(\rho, \phi)}{H_z(\rho, \phi)} \right| = \frac{\beta}{k_c^2 \rho \tan(\phi)}$$
$$H_{total}^2(\rho, \phi) = \left[\left(\frac{\beta}{k_c^2 \rho \tan(\phi)} \right)^2 + 1 \right] H_z^2(\rho, \phi) = \left[\left(\frac{\beta}{k_c^2 \rho \tan(\phi)} \right)^2 + 1 \right] \sin^2(\phi) H_z^2(\rho)$$
$$P_{loss}(\rho) = \frac{R_s}{2} \int_0^{2\pi} H_{total}^2(\rho, \phi) \rho d\phi = \frac{R_s \rho H_z^2(\rho)}{2} \int_0^{2\pi} \left[\left(\frac{\beta}{k_c^2 \rho} \right)^2 \cos^2 \phi + \sin^2 \phi \right] d\phi$$
$$= \frac{R_s H_z^2(\rho) \rho \pi}{2} \left[\left(\frac{\beta}{k_c^2 \rho} \right)^2 + 1 \right] \tag{B1}$$

On the surfaces, the electromagnetic field is given in Eq. (B2):

$$E_z(a, \phi) = E_z(b, \phi) = 0 \quad \frac{H_z(a, \phi)}{H_z(b, \phi)} = \frac{CJ_1(k_c a) + DY_1(k_c a)}{CJ_1(k_c b) + DY_1(k_c b)}$$

$$E_\phi(a, \phi) = E_\phi(b, \phi) = 0 \quad \frac{E_\rho(a, \phi)}{E_\rho(b, \phi)} = \frac{CJ_1(k_c a) + DY_1(k_c a)}{CJ_1(k_c b) + DY_1(k_c b)} \times \frac{b}{a}$$

$$H_\rho(a, \phi) = H_\rho(b, \phi) = 0 \quad \frac{H_\phi(a, \phi)}{H_\phi(b, \phi)} = \frac{CJ_1(k_c a) + DY_1(k_c a)}{CJ_1(k_c b) + DY_1(k_c b)} \times \frac{b}{a} \tag{B2}$$

$$\text{where } \frac{CJ_1(k_c a) + DY_1(k_c a)}{CJ_1(k_c b) + DY_1(k_c b)} < 1$$

$$\text{and } \frac{CJ_1(k_c a) + DY_1(k_c a)}{CJ_1(k_c b) + DY_1(k_c b)} \times \frac{b}{a} > 1$$

From the equations above, we find that the Hz field component on the inner conductor is lower than that of the outer conductor. The H_ϕ component has the opposite trend. β determines the ratio between H_ϕ and H_z. A smaller β reduces the contribution of H_ϕ to the total H field. It suggests that k should be close to the k_c, and the impedance should be preferably high, and this sets up the design optimization criteria.

The loss on inner and outer conductor ratio can be given in Eq. (B3):

$$\frac{P_a}{P_b} = \frac{H_{total}^2(a) \times a}{H_{total}^2(b) \times b} = \frac{a \times \left[\left(\frac{\beta}{k_c^2 a}\right)^2 + 1\right]}{b \times \left[\left(\frac{\beta}{k_c^2 b}\right)^2 + 1\right]} \times \frac{H_z^2(a)}{H_z^2(b)} \tag{B3}$$

In a practical consideration, we fix the outer radius and change the inner radius a, and we plot P_a/P_b as a function of a/b for both types of couplers in Fig. B1. The amplitude is normalized to the power loss on the outer conductor surface. This figure suggests that we reverse the power loss ratio from b/a in TEM mode into a/b in TE$_{11}$ couplers. Also, a small a/b is preferable in a TE$_{11}$ coupler.
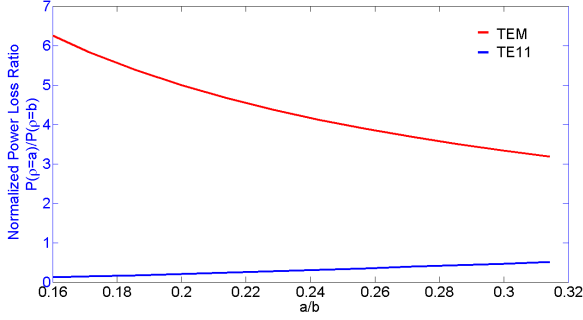

Figure B1. RF loss ratio between inner and outer surfaces on TE$_{11}$ (blue) and TEM (red) modes are plotted as a function of ρ in a coaxial coupler. The unit are arbitrary.
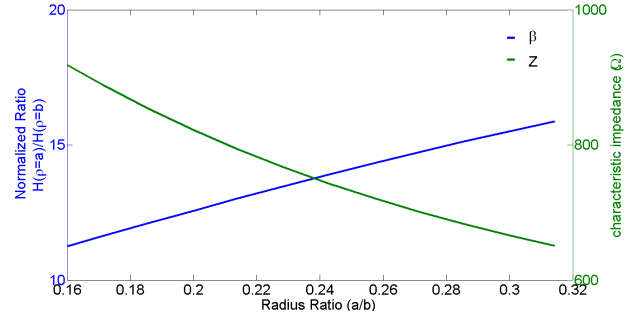
Figure B2. Characteristic impedance Z and propagation constant β is plotted as a function of the a/b.

Moreover, we change the impedance and present it in Fig. B2. It suggests that a small a/b is preferable to minimize β and increase the characteristic impedance Z.

In our case, the inner and outer conductor radii are $15\,\text{mm}$ and $70\,\text{mm}$, $a/b = 0.214$. Numerically we got k_c equal to $24.1\,\text{m}^{-1}$, and k is $27.41\,\text{m}^{-1}$ for $1.3\,\text{GHz}$ frequency. We put those numbers into the equations and obtained Eq. (B4).

$$Z = \frac{E_\rho}{H_\phi} = \frac{\eta k}{\beta} = \frac{\eta \times k}{\sqrt{k^2 - k_c^2}} = \frac{377 \times 27.41}{13.03} = 793.3\,\Omega \tag{B4}$$

We also obtained γ equal to -0.1013. For any ϕ, the electromagnetic field components on both conductor surfaces are given in Eq. (B5): (normalized to A)

$$E_z(a,\phi) = E_z(b,\phi) = 0 \quad \frac{H_z(a,\phi)}{H_z(b,\phi)} = 0.6178$$

$$E_\phi(a,\phi) = E_\phi(b,\phi) = 0 \quad \frac{E_\rho(a,\phi)}{E_\rho(b,\phi)} = 0.6178 \times \frac{b}{a} = 3.0120 \tag{B5}$$

$$H_\rho(a,\phi) = H_\rho(b,\phi) = 0 \quad \frac{H_\phi(a,\phi)}{H_\phi(b,\phi)} = 0.6178 \times \frac{b}{a} = 3.0120$$

$$\frac{P_a}{P_b} = \frac{0.015\,\text{m} \times \left[\left(\frac{13.03\,\text{m}^{-1}}{(24.1\,\text{m}^{-1})^2 \times 0.015\,\text{m}}\right)^2 + 1\right]}{0.070\,\text{m} \times \left[\left(\frac{13.03\,\text{m}^{-1}}{(24.1\,\text{m}^{-1})^2 \times 0.070\,\text{m}}\right)^2 + 1\right]} \times 0.6178^2 = 0.2396 \approx \frac{b}{a} \tag{B6}$$

Because of the lower H field and smaller surface area, the surface loss on inner radius would be smaller than that of the outer conductor. For a comparison, TEM mode has low H_z components in the couplers. The electric and magnetic fields are demonstrated in Eq. (B6).

$$H_\phi = \frac{A}{2\pi\rho} e^{-\beta z}$$
$$E_\rho = \frac{AZ}{\rho \ln \frac{b}{a}} e^{-\beta z}$$
$$\overrightarrow{H_{total}} = \overrightarrow{H_\phi} \tag{B7}$$
$$\frac{P_a}{P_b} = \frac{H_{total}^2(\rho) \times a}{H_{total}^2(\rho) \times b} = \frac{b}{a}$$

The H field is dominated by H_ϕ, which makes the inner conductor loss bigger than that of the outer conductor.

APPENDIX C. TOTAL RF ATTENUATION RATE

In a TE_{11} coaxial cable, the power flows in the coaxial coupler mode are given in Eq. (C1).

$$
\begin{aligned}
P_{In} &= \frac{1}{2}\text{Re} \int_{\rho=a}^{b} \int_{\phi=0}^{2\pi} \bar{E} \times \bar{H}^* \cdot \hat{z}\rho\, d\phi\, d\rho \\
&= \frac{1}{2}\text{Re} \int_{\rho=a}^{b} \int_{\phi=0}^{2\pi} [E_\rho H_\phi^* - E_\phi H_\rho^*]\rho\, d\phi\, d\rho \\
&= \frac{\omega\mu A'^2 \text{Re}(\beta)}{2k_c^4} \int_{\rho=a}^{b} \int_{\phi=0}^{2\pi} \left[\frac{1}{\rho^2}\cos^2\phi(J_1(k_c\rho) + \gamma Y_1(k_c\rho))^2 + k_c^2\sin^2\phi(J'_1(k_c\rho) + \gamma Y'_1(k_c\rho))^2\right]\rho\, d\phi\, d\rho \\
&= \frac{\omega\mu A'^2 \text{Re}(\beta)}{4k_c^4} \int_{\rho=a}^{b} \left[\frac{1}{\rho}(J_1(k_c\rho) + \gamma Y_1(k_c\rho))^2 + \rho k_c^2(J'_1(k_c\rho) + \gamma Y'_1(k_c\rho))^2\right] d\rho \\
&= \frac{\omega\mu A'^2 \text{Re}(\beta)}{4k_c^4} \left\{\int_{\rho=a}^{b} \left\{\left[\frac{1}{\rho}(J_1^2(k_c\rho) + \rho k_c^2 J'^2_1(k_c\rho)\right] + \gamma\left[\frac{1}{\rho}(Y_1^2(k_c\rho) + \rho k_c^2 Y'^2_1(k_c\rho)\right] d\rho + \ldots \right. \\
&\quad \left. \ldots + \int_{\rho=a}^{b} 2\gamma\left[\frac{1}{\rho}(J_1(k_c\rho)Y_1(k_c\rho) + \rho k_c^2 J'_1(k_c\rho)Y'_1(k_c\rho)\right] d\rho\right\} \\
&\because \int_{\rho=0}^{p'_{mn}} \frac{1}{\rho}J_1^2(p'_{mn}\rho) + \rho p'^2_{mn} J'^2_1(p'_{mn}\rho)d\rho = (p'^2_{mn} - 1)J_1^2(p'_{mn}) \\
&= \frac{\omega\mu\pi A'^2\beta}{4k_c^4} \left[J_1^2(k_cb) + \gamma Y_1^2(k_cb)\right]\left[(k_cb)^2 - 1\right] - \left[J_1^2(k_ca) + \gamma Y_1^2(k_ca)\right]\left[(k_ca)^2 - 1\right] + \ldots
\end{aligned}
$$

$$+2\gamma \left\{ J_1(k_cb)Y_1(k_cb)\left[(k_cb)^2 - 1\right] - J_1(k_ca)Y_1(k_ca)\left[(k_ca)^2 - 1\right] \right\}$$

$$= \frac{\omega\mu\pi A'^2\beta}{4k_c^4}\left\{ [\nabla(b)]^2\left[(k_cb)^2 - 1\right] - [\nabla(a)]^2\left[(k_ca)^2 - 1\right] \right\}$$

$$\text{where} \quad \nabla(\rho) = J_1(k_c\rho) + \gamma Y_1(k_c\rho) \tag{C1}$$

We also obtained the amplitude A' value, respected to the input P shown in Eq. (C2).

$$A'^2 = \frac{4k_c^4 P_{in}}{\omega\mu\pi\beta\left\{ [\nabla(b)]^2\left[(k_cb)^2 - 1\right] - [\nabla(a)]^2\left[(k_ca)^2 - 1\right] \right\}} \tag{C2}$$

While the power dissipated on the RF surfaces, a unit length can be illustrated in Eq. (C3).

$$P_{loss} = \frac{R_s}{2}\text{Re}\left[\int_{\phi=0}^{2\pi}\bar{H}^2 a d\phi + \int_{\phi=0}^{2\pi}\bar{H}^2 b d\phi\right]$$

$$= R_s\pi\text{Re}\left\{\int_{\phi=0}^{2\pi}\left[|H|_\phi^2 + |H|_z^2\right]a d\phi + \int_{\phi=0}^{2\pi}\left[|H|_\phi^2 + |H|_z^2\right]b d\phi\right\}$$

$$= \frac{A'^2 R_s}{2}\text{Re}\left\{\int_{\phi=0}^{2\pi}\left[\frac{\beta^2}{k_c^4\rho^2}\cos^2\phi + \sin^2\phi\right](J_1(k_ca) + \gamma Y_1(k_ca))^2 a d\phi + \dots\right.$$

$$\left.\int_{\phi=0}^{2\pi}\left[\frac{\beta^2}{k_c^4\rho^2}\cos^2\phi + \sin^2\phi\right](J_1(k_cb) + \gamma Y_1(k_cb))^2 b d\phi\right\}$$

$$= \frac{A'^2 R_s\pi}{2}\left\{a\left[1 + \frac{\beta^2}{k_c^4 a^2}\right](J_1(k_ca) + \gamma Y_1(k_ca))^2 + b\left[1 + \frac{\beta^2}{k_c^4 b^2}\right](J_1(k_cb) + \gamma Y_1(k_cb))^2\right\}$$

$$= \frac{A'^2 R_s\pi}{2}\left\{a\left[1 + \frac{\beta^2}{k_c^4 a^2}\right]\nabla(a)^2 + b\left[1 + \frac{\beta^2}{k_c^4 b^2}\right]\nabla(b)^2\right\} \tag{C3}$$

The attenuation rate will be given in Eq. (C4):

$$\alpha_{TE11} = \frac{P_{loss}}{2P_{In}} = \frac{\dfrac{A'^2 R_s\pi}{2}\left\{a\left[1 + \dfrac{\beta^2}{k_c^4 a^2}\right]\nabla(a)^2 + b\left[1 + \dfrac{\beta^2}{k_c^4 b^2}\right]\nabla(b)^2\right\}}{\dfrac{\omega\mu\pi A'^2\beta}{2k_c^4}\left\{\nabla(b)^2\left[(k_cb)^2 - 1\right] - \nabla(a)^2\left[(k_ca)^2 - 1\right]\right\}}$$

$$= \frac{R_s\left\{a\left[k_c^4 + \dfrac{\beta^2}{a^2}\right]\nabla(a)^2 + b\left[k_c^4 + \dfrac{\beta^2}{b^2}\right]\nabla(b)^2\right\}}{\eta k\beta\left\{\nabla(b)^2\left[(k_cb)^2 - 1\right] - \nabla(a)^2\left[(k_ca)^2 - 1\right]\right\}} \tag{C4}$$

The loss rate could be solved numerically, and the results are the same as above. Compared with attenuation rate of TEM mode in Eq. (1), the attenuation rate ratio is given in Eq. (C5).

$$\frac{\alpha_{TEM}}{\alpha_{TE11}} = \frac{\dfrac{R_s}{2\eta}\dfrac{a^{-1} + b^{-1}}{\ln\dfrac{b}{a}}}{\dfrac{\pi R_s\left\{a\left[k_c^4 + \dfrac{\beta^2}{a^2}\right]\nabla(a)^2 + b\left[k_c^4 + \dfrac{\beta^2}{b^2}\right]\nabla(b)^2\right\}}{\eta k\beta\left\{\nabla(b)^2\left[(k_cb)^2 - 1\right] - \nabla(a)^2\left[(k_ca)^2 - 1\right]\right\}}}$$

$$= \frac{k\beta\left(a^{-1}+b^{-1}\right)\left\{\nabla(b)^2\left[(k_c b)^2-1\right]-\nabla(a)^2\left[(k_c a)^2-1\right]\right\}}{2\pi\ln\dfrac{b}{a}\left\{a\left[k_c^4+\dfrac{\beta^2}{a^2}\right]\nabla(a)^2+b\left[k_c^4+\dfrac{\beta^2}{b^2}\right]\nabla(b)^2\right\}} \tag{C5}$$

Also keeping the outer conductor with a constant, we plot the attenuation rate ratio as a function of a/b numerically in Fig. C1. The results suggest that the losses are comparable for TEM and TE$_{11}$ couplers when a/b is small. When a/b increases, the total loss increases more from TE$_{11}$ couplers. Thus, our design prefers a small a/b.
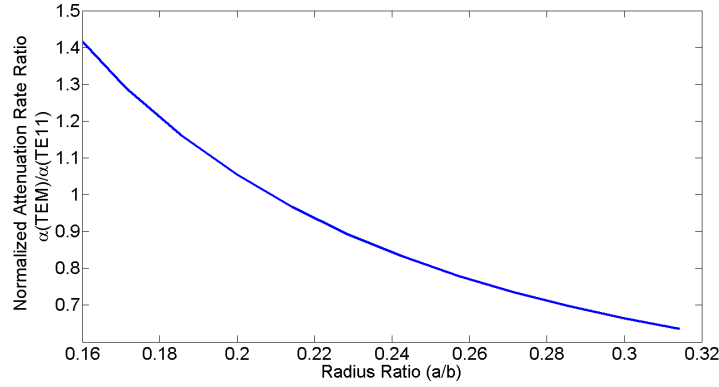

Figure C1. Attenuation rate ratio between TE$_{11}$ and TEM mode. The TE$_{11}$ couplers generate slightly more RF loss than TEM mode at the same level forward RF power when a/b are small.

APPENDIX D. PEAK ELECTRIC FIELD

Now we discuss the E total in TE$_{11}$ couplers, which is expressed in Eq. (D1).

$$\begin{aligned}
E_z(\rho,\phi) &= 0 \\
E_\rho(\rho,\phi) &= -\frac{i\omega\mu}{k_c^2\rho}A'\cos n\phi\times\left(J_1(k_c\rho)+\gamma Y_1(k_c\rho)\right) \\
E_\phi(\rho,\phi) &= \frac{i\omega\mu}{k_c}A'\sin n\phi\times\left(J_1'(k_c\rho)+\gamma Y_1'(k_c\rho)\right)
\end{aligned} \tag{D1}$$

Like TEM mode, the maximum E occurs at the inner conductor surface. Along the radial direction, E_ρ always dominates the total E field. Therefore, the maximum E total is given in Eq. (D2).

$$\begin{aligned}
E_{peak} &= E_\rho(a,\phi) = -\frac{i\omega\mu}{k_c^2 a}A'\cos n\phi\times\left(J_1(k_c a)+\gamma Y_1(k_c a)\right) \\
A'^2 &= \frac{4k_c^4 P_{in}}{\omega\mu\beta\pi\left\{\nabla(b)^2\left[(k_c b)^2-1\right]-\nabla(a)^2\left[(k_c a)^2-1\right]\right\}} \\
E_{peak} &= \frac{2}{\Delta^{\frac{1}{2}}}\sqrt{\frac{P_{in}}{\pi\omega\mu\beta}}\times\frac{\omega\mu}{a}\nabla(a) = \frac{2\nabla(a)}{\Delta^{\frac{1}{2}}}\sqrt{\frac{k\eta P_{in}}{a^2\pi\beta}} \\
\text{where}\quad \Delta &= \nabla(b)^2\left[(k_c b)^2-1\right]-\nabla(a)^2\left[(k_c a)^2-1\right]
\end{aligned} \tag{D2}$$

Similarly, we compare the E peak fields from both TEM and TE$_{11}$ modes. The ratio is given in Eq. (D3).

$$\frac{E_{peak}(TEM)}{E_{peak}(TE_{11})} = \frac{\sqrt{\dfrac{\eta P_{in}}{\pi a^2\ln\dfrac{b}{a}}}}{\dfrac{2\nabla(a)}{\Delta^{\frac{1}{2}}}\sqrt{\dfrac{k\eta P_{in}}{\pi a^2\beta}}} = \frac{\Delta^{\frac{1}{2}}}{2\nabla(a)}\sqrt{\frac{\beta}{k\ln\dfrac{b}{a}}} \tag{D3}$$
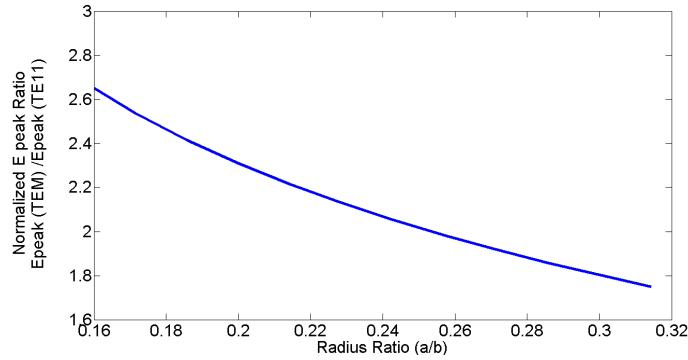
Figure D1. Peak E of both couplers at the same forward RF power are plotted as a function of a/b.

We plot this ratio as a function of a/b in Fig. D1. This figure suggests that a larger a/b will help to reduce the peak E field in the TE_{11} couplers when they transmit the same level forward RF power, because the E peak ratio is inversely proportional to beta. The maximum E_{peak} of TE_{11} and TEM modes are comparable when the same RF power are transmitted. There is not much advantage of TE_{11} mode in this case.

Another choice is that changing $b = 70 \, \text{mm}$, we still vary the a/b by changing the a. We obtained them in Fig. D2. A: $\frac{P_a}{P_b}$. B: $\frac{\alpha_{TEM}}{\alpha_{TE_{11}}}$. C: $\frac{E_{peak}(TEM)}{E_{peak}(TE_{11})}$.
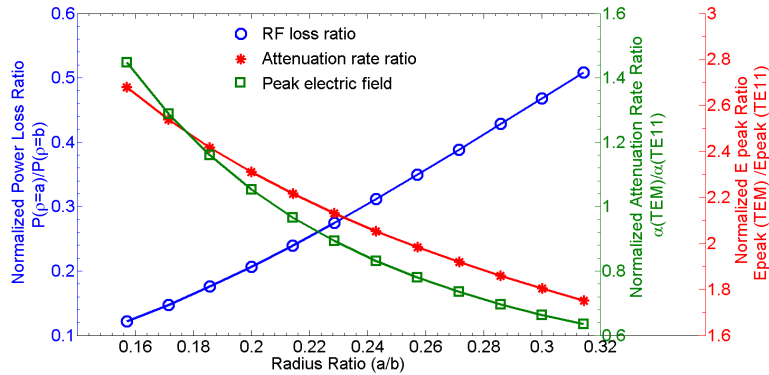

Figure D2. RF loss ratio between inner and outer surfaces (blue circle), the attenuation rate ratio (green square) and the peak electric field (red star) of both couplers at the same forward RF power are plotted as a function of radius ratio a/b.

ACKNOWLEDGMENT

REFERENCES

1. Padamsee, H., J. Knobloch, and T. Hays, *RF Superconductivity for Accelerators*, 2nd Edition, Wiley and Sons, New York, NY, 2013.
2. Campisi, I. E., et al., "The fundamental power coupler prototype for the Spallation Neutron Source (SNS) superconducting cavities," *Proceedings of the 2001 Particle Accelerator Conference*, 1140–1142, Vol. 2, Chicago, IL, 2001.

3. Belomestnykh, S., "Overview of input power coupler developments, pulsed and CW," *Proceedings of 13th International Workshop on RF Superconductivity*, Beijing, China, Jul. 2007.

4. Stirbet, M., et al., "Fundamental power coupler developments for the SNS SC linac cavities," *Proceedings of LINAC 2002*, 728–730, Gyeongju, Korea, 2002.

5. Veshcherevich, V., S. Belomestnykh, M. Liepe, V. Medjidzade, H. Padamsee, and V. Shemelin, "Design of high power input coupler for Cornell ERL injector cavities," *Proceedings of International Workshop on RF Superconductivity 2005*, 2355–2357, Ithaca, NY, USA, 2005.

6. Sakai, H., "overview of CW input couplers for ERL," *Proceedings of International Workshop on RF Superconductivity 2011*, 951–955, Chicago, IL, USA, 2011.

7. Kako, E., S. Noguchi, T. Shishido, K. Watanabe, and Y. Yamamoto, "High power tests of CW input couplers for CERL injector cryomodule," *Proceedings of International Particle Accelerator Conference 2012*, 2230–2232, New Orleans, Louisiana, USA, 2012.

8. Khan, V. F., W. Anders, A. Burrill, J. Knobloch, O. Kugeler, and A. Neumann, "RF input power couplers for high current SRF applications," *Proceedings of LINAC 2014*, 575–577, Geneva, Switzerland, 2014.

9. Pozar, D. M., *Microwave Engineering*, 4th Edition, Wiley and Sons, New York, NY, 2011.

10. Ko, K., "Advances in parallel electromagnetic codes for accelerator science and development," *Proceedings of LINAC 2010*, 1028–1030, Tsukuba, Japan, 2010.

11. Qian, H., et al., "Design of a 1.3 GHz two-cell buncher for APEX," *Proceedings of International Particle Accelerator Conference 2014*, 3924–3926, Dresden, German, 2014.

12. Rampnoux, E., et al., "Design of 352.21 MHz RF power input coupler and window for the european spallation source project (ESS)," *Proceedings of International Workshop on RF Superconductivity 2013*, 1069–1072, Paris, France, 2013.

13. Gabbott, P., *Principles and Applications of Thermal Analysis*, John Wiley & Sons, New York, NY, 2008.

14. Schultheiss, T., et al., "A high thermal conductivity waveguide window for use in a free electron laser," *Proceedings of Particle Accelerator Conference 1999*, 780–782, New York, NY, USA, 1999.

15. Galayda, J., "LCLS-II final design report," SLAC National Laboratory Report No LCLSII-1.1-DR-0251-R0, 2014.

16. Shemelin, V., S. Belomestnykh, R. L. Geng, M. Liepe, and H. Padamsec, "Dipole-mode-free and kick-free 2-cell cavity for the SC ERL injector," *Proceedings of Particle Accelerator Conference 2003*, 2059–2061, Portland, OR, USA, 2003.

17. Xu, C., S. A. Belomestnykh, W. Xu, and I. Ben-Zvi, "Second harmonic cavity design for synchrotron radiation energy compensator in ERHIC project," *Proceedings of International Workshop on RF Superconductivity 2015*, 1052–1055, Whistler, BC, Canada, 2015.

18. Kang, Y., S. Kim, and M. Doleans, "Electromagnetic simulations and properties of the fundamental power couplers for the SNS superconducting cavities," *Proceedings of Particle Accelerator Conference 2003*, 1122–1124, Chicago, IL, 2001.